Available online at www.sciencedirect.com
SCIENCE DIRECT
Journal of Power Sources 154 (2006) 74–85
JOURNAL OF POWER SOURCES
www.elsevier.com/locate/jpowsour

Mechanistic modelling of a cathode-supported tubular solid oxide fuel cell

R. Suwanwarangkul [a], E. Croiset [a,*], M.D. Pritzker [a], M.W. Fowler [a], P.L. Douglas [a], E. Entchev [b]

[a] *Department of Chemical Engineering, University of Waterloo, 200 University Avenue West, Waterloo, Ont., Canada N2L 3G1*
[b] *Advanced Combustion Technologies Laboratory, CANMET Energy Technology Centre, 1 Haanel Drive, Ottawa, Ont., Canada K1A 1M1*

Received 11 December 2004; accepted 7 March 2005
Available online 1 July 2005

Abstract

A two-dimensional mechanistic model of a tubular solid oxide fuel cell (SOFC) considering momentum, energy, mass and charge transport is developed. The model geometry of a single cell comprises an air-preheating tube, air channel, fuel channel, anode, cathode and electrolyte layers. The heat radiation between cell and air-preheating tube is also incorporated into the model. This allows the model to predict heat transfer between the cell and air-preheating tube accurately. The model is validated and shows good agreement with literature data. It is anticipated that this model can be used to help develop efficient fuel cell designs and set operating variables under practical conditions. The transport phenomena inside the cell, including gas flow behaviour, temperature, overpotential, current density and species concentration, are analysed and discussed in detail. Fuel and air velocities are found to vary along flow passages depending on the local temperature and species concentrations. This model demonstrates the importance of incorporating heat radiation into a tubular SOFC model. Furthermore, the model shows that the overall cell performance is limited by O_2 diffusion through the thick porous cathode and points to the development of new cathode materials and designs being important avenues to enhance cell performance.

Keywords: Mechanistic modelling; Tubular SOFC; Cathode-supported; Momentum transport; Heat/mass transport; Charge transport

1. Introduction

Tubular solid oxide fuel cells (SOFCs) are considered to be the most advanced design for mid- to large-scale applications up to 2 MW [1]. However, due to the complex interactions of several physical phenomena, rigorous mathematical models are required to analyse the impact of cell design and operating conditions on the cell performance.

Over the recent years, various SOFC models have been developed. Campanari [2] developed a tubular cell model from a thermodynamic point of view and included the impacts of thermodynamic non-idealities on cell performance in terms of parameter correlations. Nagata et al. [3] developed a 1D steady-state tubular SOFC model considering electrochemical and internal reforming reactions. They divided the cell into many control volumes that behave as continuous stirred tank reactors (CSTRs). Unfortunately, the model simplifies the actual cell geometry within a stack and the calculation of heat transfer coefficient is also based on fully developed laminar flow at a constant heat flux. Aguiar et al. [4,5] developed models for direct- and indirect-internal reforming of CH_4. However, they used various correlations to determine mass flux, heat flux and cell resistance that are specific to particular operating conditions. Moreover, they assumed uniform distributions of species concentrations and heat along the radial direction. This implies that the

* Corresponding author. Tel.: +1 519 888 4567x6472; fax: +1 519 746 4979.
E-mail address: ecroiset@uwaterloo.ca (E. Croiset).

0378-7753/$ – see front matter © 2005 Elsevier B.V. All rights reserved.
doi:10.1016/j.jpowsour.2005.03.197

Nomenclature

A	area perpendicular to the current flow (m^2)
B_o	parameter defined by Carman–Kozeny equations
c	molar concentration (kmol m^{-3})
C_p	molar specific heat (J $kg\,mol^{-1}\,K^{-1}$)
D_{ij}	binary diffusivity of a species i into another species j ($m^2\,s^{-1}$)
$D_{i,k}^{eff}$	effective Knudsen diffusivity of a species i through porous media ($m^2\,s^{-1}$)
D_i	mass diffusion coefficient of species i ($m^2\,s^{-1}$)
$D_{O_2}^{eff}$	effective diffusivity through the porous cathode
d_p	particle diameter (m)
E^0	reversible cell potential (V)
F	Faraday's constant (96 487 A s mol^{-1})
F_r	correction factor for heat radiation
I_{An}, I_{Cat}	current along the peripheral path of anode and cathode, respectively (A)
I_E	current density through each cell radial segment ($A\,m^{-2}$)
J	current density (mA cm^{-2})
K	equilibrium constant
L	cell length (m)
L_{path}	path length along peripheral segment of electrodes (m)
M	molecular weight (kg $kmol^{-1}$)
$\vec{m}$	mass flux (kg $m^{-2}\,s^{-1}$)
$\vec{N}$	molar flux (kmol $m^{-2}\,s^{-1}$)
p	pressure (Pa)
P_w	partial pressure of water (millibars)
Q	volumetric heating rate ($W\,m^{-3}$)
R	gas constant (8.31441 J $mol^{-1}\,K^{-1}$)
r	radial coordinate (m)
R_{Cat}, R_{An}	discretized electrical resistance of the cathode and the anode, respectively (Ω)
s	electrode interface conductivity ($\Omega^{-1}\,cm^{-2}$)
S_j	volumetric rate of generation of species j (kmol $m^{-3}\,s^{-1}$)
T	temperature (K)
u, v	velocity in radial and axial directions, respectively ($m\,s^{-1}$)
y	mole fraction
z	axial coordinate (m)

Greek letters

ε	emissivity factor
$\bar{\phi}_{An}$, $\bar{\phi}_{Cat}$	average potentials at the anode and the cathode, respectively (V)
ΔH_{elec}	enthalpy generation due to electrochemical reaction (kJ mol^{-1})
η	overpotential (V)
λ	thermal conductivity ($W\,m^{-1}\,K^{-1}$)
μ	dynamic viscosity ($N\,m^{-1}\,s^{-1}$)
ϕ	potential (V)
φ	porosity
ρ	gas density (kg m^{-3})
σ	electrical conductivity ($\Omega^{-1}\,m^{-1}$)
σ_o	Stefan–Boltzmann constant ($5.67 \times 10^{-8}\,W\,m^{-1}\,K^{-4}$)
τ_M, τ_K	tortuosity factors for molecular and Knudsen diffusion, respectively

Subscripts and superscripts

AC	air channel
An	anode
APT	air-preheating tube
Cat	cathode
E	electrolyte
H_2	hydrogen
H_2O	water
N_2	nitrogen
O_2	oxygen

concentration resistances caused by mass diffusion through the porous electrodes are negligible. The most recent and advanced models for a tubular SOFC have been presented by Li and Chyu [6] and Li and Suzuki [7]. These models account for the actual geometry of the cell and all major phenomena, including momentum, heat and mass transport coupled with electrochemical and chemical reactions. Unfortunately, these models neglect the diffusion of oxygen through the thick porous cathode. Since the O_2 diffusivity is much less than the H_2 diffusivity, the overall cell performance is limited by the O_2 diffusion through the porous electrode to reach the reaction site at the cathode/electrolyte interface. Furthermore, the rates of the electrochemical reactions are expressed entirely in terms of exchange current densities as adopted from Chan et al. [8] and are assumed to remain constant along the cell length. This assumption can cause serious errors in the determination of the current density profile along the cell length since the kinetics of electrochemical reactions strongly depend on temperature and local species concentrations [3,9,10]. Thus, the exchange current density must vary along the cell length. Finally, the effect of heat radiation was not incorporated by Li and Suzuki [7]. Although the model of Li and Chyu [6] considered heat radiation, the method for incorporating surface radiant exchange was unclear. Campanari and Iora [11] developed a tubular SOFC model supplied by methane-reformed gases. Unfortunately, the momentum transport was not incorporated into this model and the calculation of heat transfer coefficients was based on constant Nusselt number for both the air and fuel sides, which is valid only when a constant heat flux is transferred to the fluid flow. However, heat generation within an SOFC depends on the rate of electrochemical reactions which is not uniform.

In the present work, a mechanistic model of a cathode-supported tubular SOFC is developed. Fuel and oxidant gases considered in this model are humidified hydrogen and air, respectively. The model geometry comprises the air and fuel channels, cathode, electrolyte, anode and air-preheating tube. Momentum, heat and mass transport equations coupled with the electrochemical reactions are solved simultaneously. Therefore, correlations for heat and mass transfer are not required. In addition, the model incorporates a number of potentially important factors: finite cathode size, mass transport of O_2 through the cathode using the dusty-gas model, dependence of the exchange current densities on temperature and concentration and radiative heat transfer between the cell and air-preheating tube.

Table 1
Dimensions of cell components and of the flow passages used in the model

Item	Value
I. Component thickness (μm)	
Supporting tube	1500
Cathode	1000
Electrolyte	50
Anode	150
II. Diameter (mm)	
Inner side of air-preheating tube	8.0
Outer side of air-preheating tube	9.0
Inner side of supporting tube	13.8
Outer side of anode	19.2
Outer diameter of fuel channel	29.2
III. Cell length (mm)	500

2. Model description

2.1. Basic features of the cell and model geometry

The cell components used in this simulation consist of supporting tube, cathode, electrolyte and anode fabricated in a tubular shape with one closed end, as illustrated in Fig. 1. The cell dimensions are taken from the work of Hagiwara et al. [12] (Table 1). For the purposes of this model development, energy and mass transport through the supporting tube are considered to be similar to those through the cathode so that no distinction is made between these components of the cell.

Due to symmetry conditions, only the portion on one side of the symmetry plane is considered in the model (Fig. 2). The anode thickness (r-direction) is not taken into account in the model geometry since mass transfer and ohmic resistances through the thin porous anode are much smaller than those through the other cell components.

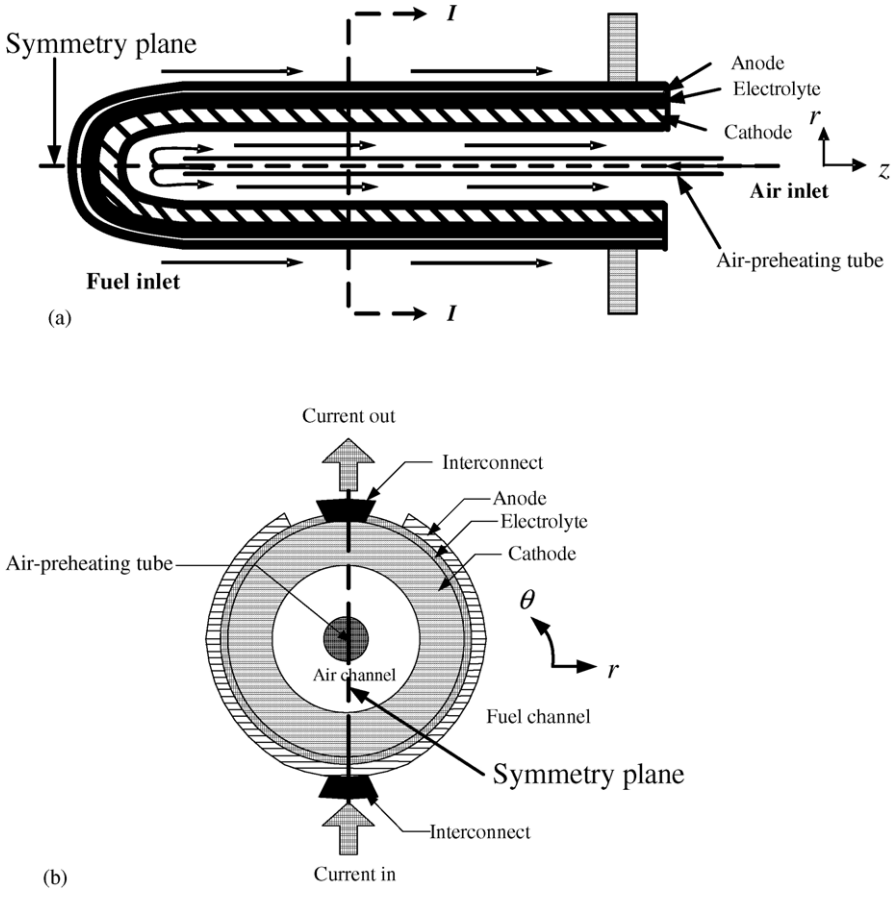

Fig. 1. Schematic diagram of a typical tubular SOFC: (a) longitudinal section of flow passages and (b) cell cross-section.

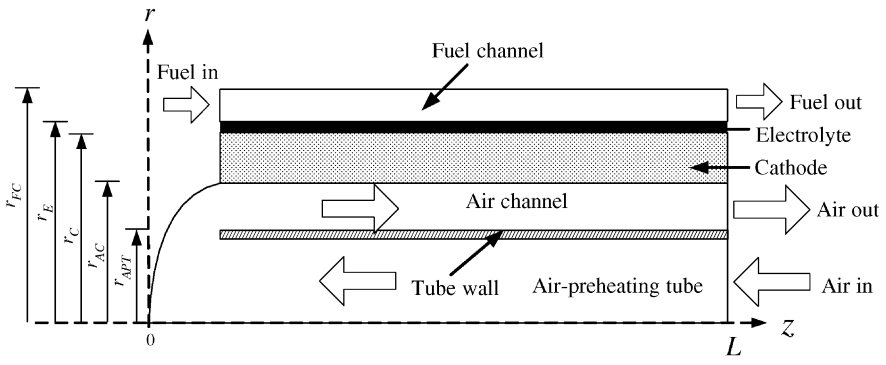

Fig. 2. Schematic diagram of the model geometry (not to scale).

Since the variation of the system properties in the azimuthal (θ)-direction is not expected to be significant, the model equations are solved in two dimensions only in the r–z plane (see Fig. 2) to determine the profiles of current densities, temperature and species concentrations along the cell length. However, since the current flows in the θ-direction as it flows from one interconnect to the other, an ohmic drop exists in this direction. This effect is incorporated in the model by coupling the equations in the r–z plane to a separate calculation of the ohmic resistance along the path of the current flow in the r–θ plane at each z-position. Some simplifications and assumptions were made in order to effectively link the calculation in the two planes, as described next.

2.2. Model assumptions

- The model is based on steady-state, non-isothermal operation using humidified H_2 as the fuel source.
- Gas flows in the channels are laminar.
- The fuel cell operates with 100% current efficiency, i.e., no reactant gas crossover or side reactions.
- There is no variation of temperature and species concentrations in the azimuthal direction within the cell.
- Heat transfer within the porous cathode occurs by conduction only, i.e., the enthalpy carried by oxygen in the pore space is negligible.
- Heat transfer by radiation occurs only between the air-preheating tube and cell structure. The radiant heat from one cell to the next cell within the stack is negligible because of geometrical symmetry, i.e., the temperature distribution along the cell length is the same from one cell to the adjacent cells.
- The mass transfer resistance through the porous anode is ignored because of its small thickness and comparatively high H_2 diffusivity.
- The ohmic drop within the cell is due to ionic resistance of the electrolyte and electronic resistance of the porous electrodes along the peripheral current path in the r–θ plane at each z-position.
- The current density along the peripheral path at the cathode is equal to that at the anode since the radius at the periphery of the cathode is similar to that of the anode.

2.3. Equivalent circuit of a tubular cell

In order to describe the flow of current and the effect of ohmic resistances on cell performance, the equivalent circuit shown in Fig. 3 is used. The flow of current from the anode interconnect to the cathode interconnect through the cell components can be described in terms of an equivalent circuit over the cross-sectional area of the cell. To determine the ohmic drop within the cathode and the anode, the peripheral path of the cell is divided into many small equal segments. The resistances of the cathode and the anode to current flow between the nodes are given as:

$$R_{\mathrm{An}} = \frac{L_{\mathrm{path,An}}}{\sigma_{\mathrm{An}} A_{\mathrm{An}}} \tag{1}$$

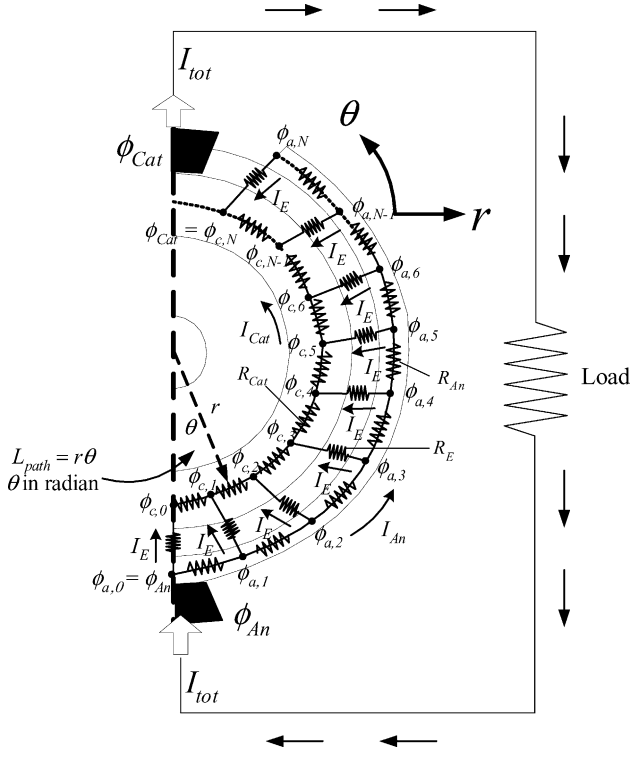

Fig. 3. Schematic diagram of equivalent circuit to account for ohmic resistances in the r–θ plane (not to scale).

$$R_{\mathrm{Cat}} = \frac{L_{\mathrm{path,Cat}}}{\sigma_{\mathrm{Cat}} A_{\mathrm{Cat}}} \tag{2}$$

where $L_{\mathrm{path,An}}$ and $L_{\mathrm{path,Cat}}$ are the path lengths along each peripheral segment of the anode and the cathode, respectively. σ_{An} and σ_{Cat} represent the conductivities of the anode and the cathode, respectively. However, in the range of SOFC operating temperature (800–1200 °C), σ_{An} and σ_{Cat} remain virtually constant [13]. A_{An} and A_{Cat} are the areas perpendicular to the flows of I_{An} and I_{Cat}, respectively.

Assuming no ohmic resistance within the interconnects, $\phi_{\mathrm{a},0}$ and $\phi_{\mathrm{c},N}$ are the same as the potentials of the anode interconnects, i.e., $\phi_{\mathrm{a},0} = \phi_{\mathrm{An}}$ and $\phi_{\mathrm{c},N} = \phi_{\mathrm{Cat}}$. Moreover, the current density flowing from the anode to the cathode (I_{E}) at every node is the same because it is determined by the electrode kinetics that are functions of temperature and species concentrations for which no angular dependence is assumed. The current balance for the anode region can be described as:

For node j, $j = 1, \ldots, N-1$:

$$\frac{\phi_{\mathrm{a},j} - \phi_{\mathrm{a},j-1}}{R_{\mathrm{An}}} - \frac{\phi_{\mathrm{a},j+1} - \phi_{\mathrm{a},j}}{R_{\mathrm{An}}} - I_{\mathrm{E}} A_{\mathrm{E}} = 0 \tag{3}$$

For node N:

$$\frac{\phi_{\mathrm{a},N} - \phi_{\mathrm{a},N-1}}{R_{\mathrm{An}}} - I_{\mathrm{E}} A_{\mathrm{E}} = 0 \tag{4}$$

The current balance of each node at the cathode region can be formulated similarly.

Although I_{E} has no angular dependence, it varies in the longitudinal direction (z-direction). It becomes computationally prohibitive to solve the anode and cathode current balances for each value of z and then use them in conjunction with the transport equations in the r- and z-directions. Consequently, the approach used is to first solve the transport equations in the r- and z-directions to obtain numerical values for the current density J_{An} (=J_{Cat}) over the entire peripheral path as a function of z. Once this is obtained, I_{E} is determined as the average value of J_{An} over the cell length L, i.e.,

$$I_{\mathrm{E}} = \frac{1}{L} \int_0^L J_{\mathrm{An}} \, \mathrm{d}z \tag{5}$$

The current balances given by Eqs. (3) and (4) are solved once using this value of I_{E} to yield one set of anodic and cathodic potentials representing the average behaviour in the axial direction.

The amount of current flowing through the electrolyte is related to the electrochemical reactions of O_2 and H_2 at the cathode/electrolyte and the anode/electrolyte interfaces, respectively. No homogeneous reactions occur within the electrolyte and transport by O^{2-} across the electrolyte occurs predominantly by migration rather than by diffusion. Thus, the distribution of the potential, ϕ_{E}, within the electrolyte is determined as follows:

$$\nabla \cdot (-\sigma_{\mathrm{E}} \nabla \phi_{\mathrm{E}}) = 0 \quad \text{or}$$

$$\frac{1}{r} \frac{\partial (r \sigma_{\mathrm{E}} \, \partial \phi_{\mathrm{E}} / \partial r)}{\partial r} + \frac{\partial (\sigma_{\mathrm{E}} \, \partial \phi_{\mathrm{E}} / \partial z)}{\partial z} = 0 \tag{6}$$

This equation can be solved numerically subject to the following boundary conditions:

$$\mathbf{n} \cdot (\sigma_{\mathrm{E}} \nabla \phi_{\mathrm{E}}) = -J_{\mathrm{An}} \quad \text{at} \quad r = r_{\mathrm{E}}$$

(anode/electrolyte interface) (7)

$$\mathbf{n} \cdot (\sigma_{\mathrm{E}} \nabla \phi_{\mathrm{E}}) = J_{\mathrm{Cat}} \quad \text{at} \quad r = r_{\mathrm{C}}$$

(cathode/electrolyte interface) (8)

where J_{Cat} and J_{An} arise due to the electrochemical reactions of O_2 reduction and H_2 oxidation, respectively, in units of A m^{-2}. These rate expressions are obtained from the work of Nagata et al. [3]:

$$J_{\mathrm{An}} = \frac{10\,000 RT}{3F} s_{\mathrm{An}} \left\{ \exp\left(\frac{2F\eta_{\mathrm{An}}}{RT} \right) - \exp\left(\frac{-F\eta_{\mathrm{An}}}{RT} \right) \right\} \tag{9}$$

$$J_{\mathrm{Cat}} = \frac{10\,000 RT}{4F} s_{\mathrm{Cat}} \left\{ \exp\left(\frac{-2F\eta_{\mathrm{Cat}}}{RT} \right) - \exp\left(\frac{2F\eta_{\mathrm{Cat}}}{RT} \right) \right\} \tag{10}$$

where η_{An} and η_{Cat} represent the anode and cathode overpotentials, respectively, i.e.,

$$\eta_{\mathrm{An}} = \bar{\phi}_{\mathrm{An}} - \phi_{\mathrm{E}} - E^0_{\mathrm{An}} \tag{11}$$

$$\eta_{\mathrm{Cat}} = \bar{\phi}_{\mathrm{Cat}} - \phi_{\mathrm{E}} - E^0_{\mathrm{Cat}} \tag{12}$$

where $\bar{\phi}_{\mathrm{An}}$ and $\bar{\phi}_{\mathrm{Cat}}$ are the average potentials at the anode and the cathode, respectively, estimated by Simpson's rule using the potentials obtained from the equivalent circuit:

$$\bar{\phi}_{\mathrm{An}} = \frac{\phi_{\mathrm{An}} + 4\phi_{\mathrm{a},1} + 2\phi_{\mathrm{a},2} + 4\phi_{\mathrm{a},3} + \cdots + 2\phi_{\mathrm{a},N-2} + 4\phi_{\mathrm{a},N-1} + \phi_{\mathrm{a},N}}{3N} \tag{13}$$

$$\bar{\phi}_{\mathrm{Cat}} = \frac{\phi_{\mathrm{c},0} + 4\phi_{\mathrm{c},1} + 2\phi_{\mathrm{c},2} + 4\phi_{\mathrm{c},3} + \cdots + 2\phi_{\mathrm{c},N-2} + 4\phi_{\mathrm{c},N-1} + \phi_{\mathrm{Cat}}}{3N} \tag{14}$$

Since the electrode resistances remain essentially constant over the range of temperatures within the SOFC, the potentials within the electrodes can be determined once I_{E} is specified. The dependence of $\phi_{\mathrm{An}} - \bar{\phi}_{\mathrm{An}}$ and $\bar{\phi}_{\mathrm{Cat}} - \phi_{\mathrm{Cat}}$ on I_{E} at temperatures between 800 and 1200 °C is shown in Fig. 4. These simple relationships were used to facilitate the numerical algorithm to solve the model.

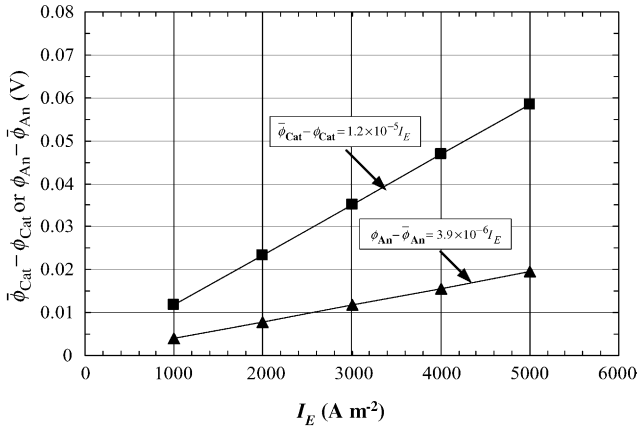

Fig. 4. Plot of $\phi_{An} - \bar{\phi}_{An}$ and $\bar{\phi}_{Cat} - \phi_{Cat}$ as a function of I_E between 800 and 1200 °C.

E^0_{An} and E^0_{Cat} are the reversible half-cell potentials of the anodic and cathodic reactions, respectively, as expressed by:

$$E^0_{An} = -\frac{RT}{4F} \ln p_{O_2,An} \quad (15)$$

$$E^0_{Cat} = -\frac{RT}{4F} \ln p_{O_2,Cat} \quad (16)$$

where $p_{O_2,An}$ and $p_{O_2,Cat}$ are partial pressures of O_2 (atm) at the anode/electrolyte and cathode/electrolyte interfaces, respectively. The former can be calculated assuming that $p_{O_2,An}$ is in chemical equilibrium with other fuel gases, and hence $p_{O_2,An}$ can be written as:

$$p_{O_2,An} = \left(\frac{p_{H_2O,An}}{K_{H_2} p_{H_2,An}}\right)^2 \quad (17)$$

where K_{H_2} is the equilibrium constant for $H_2 + 1/2O_2 \rightarrow H_2O$ which depends on temperature.

The terms s_{Cat} and s_{An} given in Eqs. (9) and (10) are estimated by the following correlations [3]:

$$s_{Cat} = 1.047 \times 10^6 \exp\left(-\frac{130\,000}{RT}\right) p^{0.50}_{O_2,Cat} \quad (18)$$

$$s_{An} = 6.166 \times 10^7 \exp\left(-\frac{120\,000}{RT}\right) p^{0.133}_{O_2,An} \quad (19)$$

2.4. Momentum, mass and energy transport equations

According to the geometry shown in Fig. 2, the equations for momentum, heat and mass transport as indicated in Eqs. (20)–(24) are solved simultaneously within the gas flow passages (air-preheating tube, air channel and fuel channel).

Overall mass balance:

$$\frac{\partial(\rho_i v_i)}{\partial z} + \frac{1}{r}\frac{\partial(r\rho_i u_i)}{\partial r} = 0 \quad (20)$$

Momentum in z-direction:

$$\frac{\partial(\rho_i v_i v_i)}{\partial z} + \frac{1}{r}\frac{\partial(r\rho_i u_i v_i)}{\partial r} = -\frac{\partial p_i}{\partial z} + \frac{\partial}{\partial z}\left(\mu_i \frac{\partial v_i}{\partial z}\right) + \frac{1}{r}\frac{\partial}{\partial r}\left(r\mu_i \frac{\partial v_i}{\partial r}\right) + \frac{\partial}{\partial z}\left(\mu_i \frac{\partial v_i}{\partial z}\right) + \frac{1}{r}\frac{\partial}{\partial r}\left(r\mu_i \frac{\partial u_i}{\partial z}\right) \quad (21)$$

Momentum in r-direction:

$$\frac{\partial(\rho_i v_i u_i)}{\partial z} + \frac{1}{r}\frac{\partial(r\rho_i u_i u_i)}{\partial r} = -\frac{\partial p_i}{\partial r} + \frac{\partial}{\partial z}\left(\mu_i \frac{\partial u_i}{\partial z}\right) + \frac{1}{r}\frac{\partial}{\partial r}\left(r\mu_i \frac{\partial u_i}{\partial r}\right) + \frac{\partial}{\partial z}\left(\mu_i \frac{\partial v_i}{\partial r}\right) + \frac{1}{r}\frac{\partial}{\partial r}\left(r\mu_i \frac{\partial u_i}{\partial r}\right) - \frac{2\mu_i u_i}{r^2} \quad (22)$$

Energy transport:

$$\frac{\partial(\rho_i C_{p_i} v_i T)}{\partial z} + \frac{1}{r}\frac{\partial(r\rho_i C_{p_i} u_i T)}{\partial r} = \frac{\partial}{\partial z}\left(\lambda_i \frac{\partial T}{\partial z}\right) + \frac{1}{r}\frac{\partial}{\partial r}\left(r\lambda_i \frac{\partial T}{\partial r}\right) + Q \quad (23)$$

Species transport:

$$\frac{\partial(c_j M_j v_i)}{\partial z} + \frac{1}{r}\frac{\partial(r c_j M_j u_i)}{\partial r} = \frac{\partial}{\partial z}\left(D_j \frac{\partial c_j}{\partial z}\right) + \frac{1}{r}\frac{\partial}{\partial r}\left(r D_j \frac{\partial c_j}{\partial r}\right) + S_j \quad (24)$$

where i denotes fuel or air and j represents H_2 in the fuel stream or O_2 in the oxidant stream. The mass diffusion coefficients, D_{H_2} and D_{O_2}, as well as the air and fuel heat capacities, are determined using the equations found in the literature [14,15].

The sink term Q in Eq. (23) and the source term S_j in Eq. (24) are set to zero because generation/consumption of heat and mass is considered to occur only at the domain boundaries. In this model, O_2 and H_2 consumption takes place at the boundaries, $r = r_C$ and r_E, respectively. Heat generation due to the electrochemical reaction is assumed to take place at $r = r_E$.

Within the porous cathode, the momentum and mass transport equations are different from the previous equations since the porous cathode is treated as a barrier to gas transport. On the other hand, the energy equation can be applied inside the porous cathode without much modification. Only the correction of the thermal conductivity to combine the properties of the cathode material, lanthanum strontium manganite (LSM) and the gas filling the pores must be made:

$$\lambda_{Cat} = \varphi_{Cat}\lambda_{air} + (1 - \varphi_{Cat})\lambda_{LSM} \quad (25)$$

where φ_{Cat} is the cathode porosity and λ_{LSM} is the thermal conductivity of the cathode material.

The most practical model widely used to describe mass transport inside porous media is *the dusty-gas model* [16–18]. This model allows for both Knudsen and bulk diffusion mechanisms in the overall diffusive flux and mass-average velocity in convective flux. The expression governing the molar flux of gas is given by:

$$\frac{-p}{RT}\nabla y_l = \frac{\vec{N}_l}{D^{\text{eff}}_{l,\text{k}}} + \sum_{l=1,m\neq l}^{n} \frac{y_m\vec{N}_l - y_l\vec{N}_m}{D^{\text{eff}}_{l-m}} + \frac{y_l}{RT}\left(1 + \frac{B_\text{o}\,p}{D^{\text{eff}}_{l,\text{k}}\mu}\right)\nabla p \tag{26}$$

where y_l and p denote mole fraction of species l and the total pressure inside porous media, respectively. $D^{\text{eff}}_{l,\text{k}}$ and D^{eff}_{l-m} are the effective Knudsen and molecular diffusivities, respectively. $\vec{N}_l$ and $\vec{N}_m$ are the molar fluxes of the participating gases. B_o characterizes the pore structure and can be determined from the Carman–Kozeny relationship [19]

$$B_\text{o} = \left(\frac{d_\text{p}^2}{72\tau}\right)\left(\frac{\varphi^3}{(1-\varphi)^2}\right) \tag{27}$$

where d_p, τ and φ are the particle size, tortuosity factor and the porosity of the porous media, respectively. The first and second terms on the right-hand side of Eq. (26) represent Knudsen and molecular diffusions, respectively, while the third term accounts for convective flow as described by Darcy's law.

With typical pore sizes and material properties of the porous cathode ($d_\text{p} = 1\,\mu\text{m}$, $\tau = 4$, $\varphi = 0.3$), B_o is estimated to be 1.91×10^{-16} and $1 + B_\text{o}p/D^{\text{eff}}_{i,\text{k}}\mu$ to be close to 1. This indicates that convective transport inside the porous cathode is insignificant. Substituting this approximation into Eq. (26) an expression used to determine O_2 mass flux is as follows:

$$\vec{m}_{\text{O}_2} = -\frac{D^{\text{eff}}_{\text{O}_2,\text{k}} D^{\text{eff}}_{\text{O}_2-\text{N}_2}}{\left[D^{\text{eff}}_{\text{O}_2-\text{N}_2} + (1 - c_{\text{O}_2}/c_\text{tot})D^{\text{eff}}_{\text{O}_2,\text{k}} + (c_{\text{O}_2}/c_\text{tot})D^{\text{eff}}_{\text{N}_2,\text{k}}\right]} M_{\text{O}_2}\nabla c_{\text{O}_2} \tag{28}$$

where c_tot is the total gas concentration in the porous cathode ($c_\text{tot} = c_{\text{N}_2} + c_{\text{O}_2}$). $D^{\text{eff}}_{\text{O}_2-\text{N}_2}$, $D^{\text{eff}}_{\text{O}_2,\text{k}}$ and $D^{\text{eff}}_{\text{N}_2,\text{k}}$ can be determined as follows:

$$D^{\text{eff}}_{\text{O}_2-\text{N}_2} = D_{\text{O}_2-\text{N}_2}\left(\frac{\varphi_\text{Cat}}{\tau_\text{M}}\right) \tag{29}$$

$$D^{\text{eff}}_{\text{O}_2,\text{k}} = D_{\text{O}_2,\text{k}}\left(\frac{\varphi_\text{Cat}}{\tau_\text{K}}\right) \tag{30}$$

$$D^{\text{eff}}_{\text{N}_2,\text{k}} = D_{\text{N}_2,\text{k}}\left(\frac{\varphi_\text{Cat}}{\tau_\text{K}}\right) \tag{31}$$

where τ_M and τ_K denote the tortuosity factors for molecular and Knudsen diffusion, respectively, and are functions of the cathode porosity. Iwata et al. [10] used the same value of τ_M and τ_K in the range of 3–6 in their mathematical model. Williford et al. [20] used a Wicke–Kallenbach experimental apparatus to estimate the tortuosity of porous anode. They found that the anode materials with typical porosities greater than 30% exhibit tortuosities in the range of 2.5–3.0, which is somewhat smaller than what Iwata et al. expected. However, in the present model, the tortuosity factors are estimated from formula based on Monte-Carlo simulations [21].

Since the O_2 reduction reaction occurs only at the cathode/electrolyte interface, the steady-state mass transport for O_2 within the cathode layer yields

$$\nabla \cdot \vec{m}_{\text{O}_2} = 0 \tag{32}$$

2.5. Boundary conditions

On the symmetrical axis at the air-preheating tube, i.e., $r = 0$: $u_\text{air} = 0$, $\partial T/\partial r = 0$, $\partial c_{\text{O}_2}/\partial r = 0$ and $\partial v_\text{air}/\partial r = 0$, and at the fuel channel, i.e., $r = r_\text{FC}$: $u_\text{fuel} = 0$, $\partial T/\partial r = 0$, $\partial c_{\text{H}_2}/\partial r = 0$ and $\partial v_\text{fuel}/\partial r = 0$. At the fuel inlet, i.e., $z = 0$, the inlet velocity, temperature and species mole fraction are prescribed by the known operating conditions. Similar inlet conditions for air are given at $z = L$. At the outlet of the air and fuel channels (i: fuel or air) at $z = L$, $p_i = 1$ atm, $\partial u_i/\partial z = 0$ and $\partial v_i/\partial z = 0$. For heat and species transport, $\partial T/\partial z = 0$, $\partial c_{\text{O}_2}/\partial z = 0$ and $\partial c_{\text{H}_2}/\partial z = 0$. At the closed end ($z = 0$), $u_\text{air} = 0$, $v_\text{air} = 0$, $T = T_\text{fuel,inlet}$ and $\nabla c_{\text{O}_2}(r, z) = 0$. Since the electrochemical reactions consume O_2 and H_2, the boundary conditions for O_2 and H_2 transport are given by $\mathbf{n}\cdot\vec{m}_{\text{O}_2} = -J_\text{Cat}M_{\text{O}_2}/4F$ at $r = r_\text{C}$ and $\mathbf{n}\cdot\vec{m}_{\text{H}_2} = -J_\text{An}M_{\text{H}_2}/2F$ at $r = r_\text{E}$, respectively. For transport within the electrolyte, the boundary conditions are $\mathbf{n}\cdot(\sigma_\text{E}\nabla\phi_\text{E}) = J_\text{Cat}$ and $\mathbf{n}\cdot(\sigma_\text{E}\nabla\phi_\text{E}) = -J_\text{An}$ at $r = r_\text{C}$ and r_E, respectively. It is assumed that the heat generation in the tubular cell is due to the exothermic electrochemical reaction at $r = r_\text{E}$. Consequently, $\mathbf{n}\cdot(\lambda_\text{E}\nabla T) = J_\text{An}[\Delta H_\text{elec}/2F + (\phi_\text{Cat} - \phi_\text{An})]$ applies at $r = r_\text{E}$, where ΔH_elec is the enthalpy change due to the overall electrochemical reaction, i.e.,

$$\Delta H_\text{elec} = \Delta H_{\text{f,H}_2\text{O}} - \Delta H_{\text{f,H}_2} - 0.5\,\Delta H_{\text{f,O}_2} \tag{33}$$

The radiative heat exchange between the surface of the cathode ($r = r_\text{AC}$) and that of the air-preheating tube ($r = r_\text{APT}$) is incorporated as boundary conditions, $\mathbf{n}\cdot(\lambda_\text{APT}\nabla T) = \sigma_\text{o}F_\text{r}(T^4|_{r=r_\text{AC}} - T^4|_{r=r_\text{APT}})$ at $r = r_\text{AC}$ and $\mathbf{n}\cdot(\lambda_\text{APT}\nabla T) = -\sigma_\text{o}F_\text{r}(T^4|_{r=r_\text{AC}} - T^4|_{r=r_\text{APT}})$ at $r = r_\text{APT}$, where F_r denotes the correction factor for heat radiation defined as [22]:

$$F_\text{r} = \frac{\varepsilon_\text{air}\varepsilon_\text{APT}(1-\varepsilon_\text{air})}{\left[1 - \left\{1 + \frac{r_\text{APT}}{r_\text{AC}}(\varepsilon_\text{Cat}\varepsilon_\text{air} - \varepsilon_\text{air} - \varepsilon_\text{Cat})\right\}(1-\varepsilon_\text{air})(1-\varepsilon_\text{APT})\right]} \tag{34}$$

where ε_air, ε_APT and ε_Cat represent the emissivities of air, air-preheating tube and cathode, respectively. ε_air strongly

depends on the amount of H_2O in air as given by [23]:

$$\varepsilon_{air} = 0.66 + 0.4P_w^{0.5} \quad (35)$$

where P_w is the partial pressure of H_2O (millibars).

2.6. Numerical implementation

The finite-element software package *FEMLAB*® [24] was used to solve the transport equations coupled with electrochemical reactions. Depending on the initial guesses for the state variables, the time required for each simulation was from 10 to 40 min on a Pentium IV 2.6 GHz. It should be noted here that the number of grid points used to discretize the geometry is a compromise between accuracy of model results and computational capacity. The grid spacing at the anode/electrolyte and cathode/electrolyte interfaces along the cell length was finer than in other regions since high gradients of temperature and species mole fractions occur in this region.

3. Results and discussion

3.1. Model validation

To ensure that the model can predict the observed behaviour of an operating tubular cell, a simulation was done to compare with the experimental data of Hagiwara et al. [12]. Physical parameters of cell components and cell operating conditions used in this simulation are summarized in Tables 2 and 3, respectively.

In this simulation, the values of fuel and air flow rates were adjusted to match the values of utilization factors given in Table 3. For different operating cell potentials, they were found to vary from ~0.002 to 0.008 kg h^{-1} for the fuel and ~0.4 to 0.9 kg h^{-1} for air. However, it is impossible to compare these values with the experimental data since they were not reported by Hagiwara et al. [12]. The current–potential plot obtained from this simulation is compared with the experimental data and the predictions from the model of Li and Suzuki [7] in Fig. 5. The present model can predict the experimentally observed dependence of current density on cell potential very well. Excellent agreement is also obtained in the low current density region where the fit of the model from Li and Suzuki [7] shows some deviation. As expected, higher current density leads to a lower cell potential due to

Table 3
Operating conditions used in this simulation

Item	Symbol	Value
Species and its molar fraction		
Hydrogen	$c_{H_2,in}$	98.6%
Water	$c_{H_2O,in}$	1.4%
Nitrogen	$c_{N_2,in}$	79.0%
Oxygen	$c_{O_2,in}$	21.0%
Inlet pressure		
Fuel	$p_{fuel,in}$	1.0135×10^5 Pa
Air	$p_{air,in}$	1.0135×10^5 Pa
Inlet temperature		
Fuel	$T_{fuel,in}$	870.0 °C
Air	$T_{air,in}$	600.0 °C
Fuel utilization	U_{fuel}	85.0%
Air utilization	U_{air}	16.7%
Cell potential	V_{cell}	0.6–0.8 V
Average current density	I_E	100–520 mA cm^{-2}

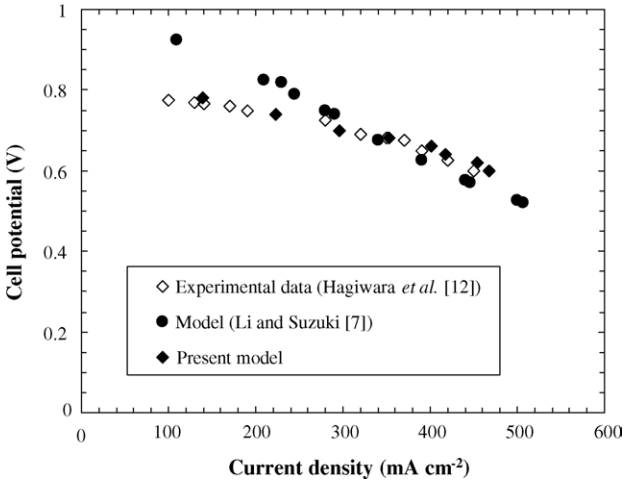

Fig. 5. Comparison of current–potential plots by the present model (♦), model from Li and Suzuki [7] (●) and the experimental data (Hagiwara et al. [12]) (◇) at $U_{air} \sim 0.167$ and $U_{fuel} \sim 0.85$.

Table 2
Physical properties of the cell components used in this simulation

Item	Symbol	Value	Reference
Cathode porosity	φ_{Cat}	0.30	[8]
Tortuosity for molecular diffusion	τ_M	1.50	[21]
Tortuosity for Knudsen diffusion	τ_K	3.44	[21]
Ionic conductivity of electrolyte	σ_E	$3.3 \times 10^4 \exp(-10\,300/T)\ \Omega^{-1}\ m^{-1}$	[13]
Electronic conductivity of cathode	σ_{Cat}	$12\,800\ \Omega^{-1}\ m^{-1}$	[13]
Electronic conductivity of anode	σ_{An}	$30\,300\ \Omega^{-1}\ m^{-1}$	[13]
Thermal conductivity of cathode	λ_{Cat}	$4\ W\ m^{-1}\ K^{-1}$	[26]
Thermal conductivity of electrolyte	λ_E	$2\ W\ m^{-1}\ K^{-1}$	[26]
Thermal conductivity of anode	λ_{An}	$2\ W\ m^{-1}\ K^{-1}$	[26]
Thermal conductivity of preheating tube	λ_{APT}	$1.1\ W\ m^{-1}\ K^{-1}$	[6]
Thermal emissivity of preheating tube	ε_{APT}	0.05	[25]
Thermal emissivity of cathode	ε_{Cat}	0.35	[25]

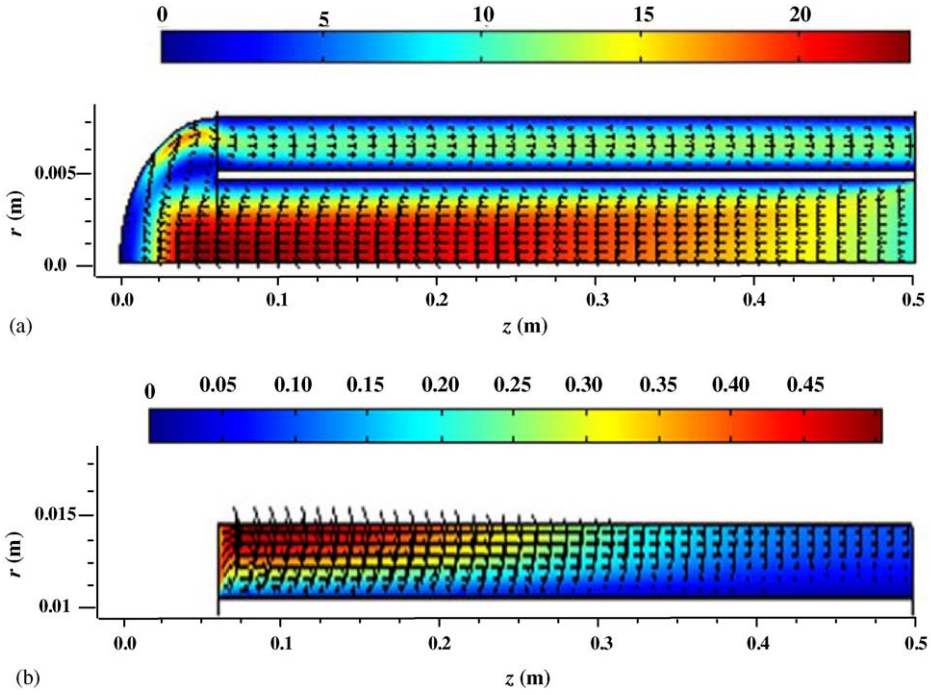

Fig. 6. Surface and arrow plots of velocity profiles for air (a) and fuel (b) inside flow passages for the base case model ($I_E \sim 300\,mA\,cm^{-2}$, $V_{cell} \sim 0.7\,V$, $U_{air} \sim 0.167$ and $U_{fuel} \sim 0.85$).

the increase in the activation, ohmic and concentration overpotentials.

3.2. Simulation results

3.2.1. Flow behaviour

The velocity profiles for air and fuel are presented in Fig. 6. The gas velocity inside the air-preheating tube increases along the tube length since air expands due to preheating (Fig. 6(a)). Once air is discharged at the closed end of the cell, it impinges on the cell wall and flows further along the air channel in the reverse direction in the annular region between the cell and the air-preheating tube. At a given mass flow rate, the velocity inside a tube is inversely proportional to the tube diameter. Accordingly, the lower velocity at the closed end of the cell is expected since the size of the closed end tube is larger than that of the air-preheating tube. Moreover, once air hits the cell wall, it loses momentum and its velocity is reduced. The velocity profile changes only slightly along the cell length outside the air-preheating tube because the temperature does not change much in this region. This is confirmed in the temperature profile along the cell length as shown in Fig. 7. Although the mass of O_2 is consumed by the electrochemical reaction along the cell length, this does not affect the air velocity profile since the total mass of air flowing through the air channel is much greater than the mass of oxygen consumed by the electrochemical reactions.

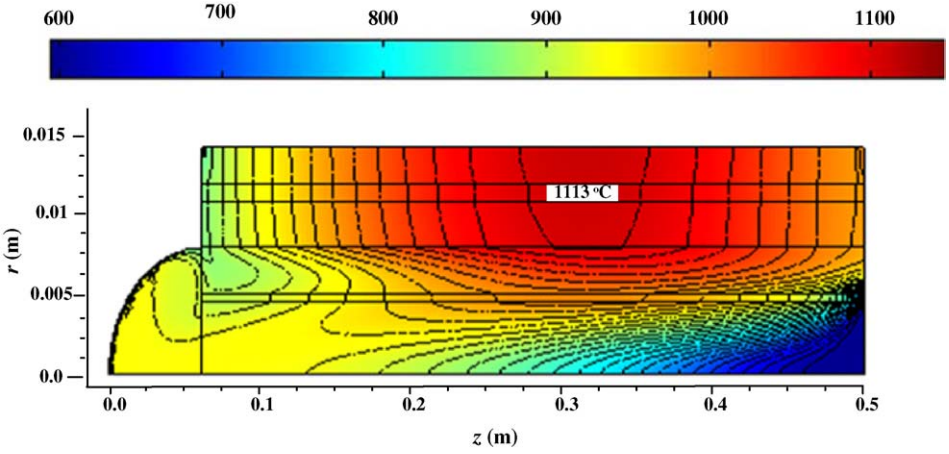

Fig. 7. Surface and contour plots of cell temperature distribution (°C) for the base case model ($I_E \sim 300\,mA\,cm^{-2}$, $V_{cell} = 0.7\,V$, $U_{air} \sim 0.167$ and $U_{fuel} \sim 0.85$).

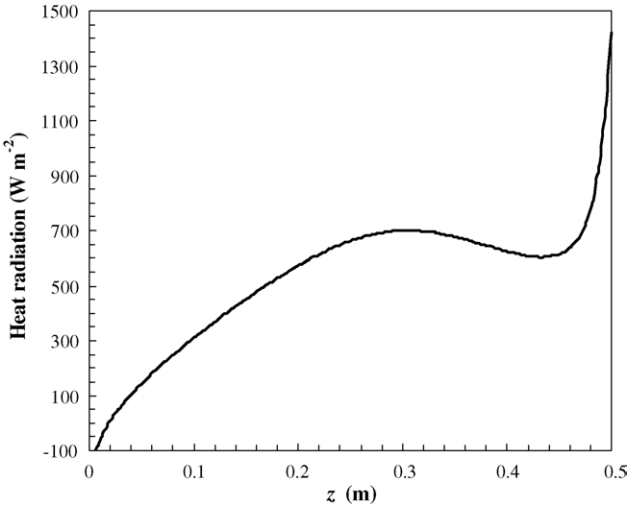

Fig. 8. Rate of radiative heat transfer from the surface of the cell to the surface of the air-preheating tube along the cell length at $r = r_{AC}$.

In contrast, the velocity profile of the fuel, as shown in Fig. 6(b), decreases along the cell length although the temperature along the cell length increases. This can be explained by the fact that H_2 is being consumed electrochemically to form water in the fuel channel. Although the molar consumption of H_2 is the same as the molar generation of H_2O, the rate of H_2O generation on a mass basis is nine times the rate of H_2 consumption. As a result, the velocity of fuel stream is reduced because of an increase in its total mass.

3.2.2. Temperature distribution

The temperature distribution is crucial to SOFC operation. The reaction kinetics strongly depends on the local cell temperature, thus affecting the overall cell performance. Furthermore, heat management is a challenging problem during cell operation. Since the cell length is quite long, cracking of the ceramic material can occur due to thermal gradients and hot spots within the cell. Consequently, this simulation focuses not only on the temperature distribution within the cell, but also on improving cell design so as to minimize temperature non-uniformity.

Fig. 7 shows the temperature distribution inside the cell. In the air-preheating tube, the air temperature increases as one approaches the closed end of the cell. The gradient is very high near the air inlet and low at the closed end of the cell before it enters the air channel. This can be explained by the fact that a high amount of heat is transferred from the cell to the preheating tube due to the exothermic electrochemical reaction. A significant rate of heat transfer occurs near the inlet of the preheating tube because of a large temperature difference between the air and the cell. When this difference is reduced, the rate of heat transfer also declines as observed near the closed end. The temperature variation within the air channel is less than that inside the air-preheating tube since the temperature difference between the air channel and the cell is not as high as that between the air-preheating tube and the cell. The radial temperature distribution within the

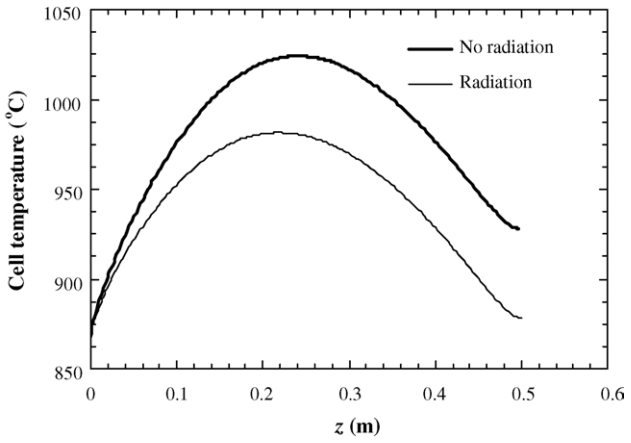

Fig. 9. Comparison of computed cell temperature profiles along the cell length between the cases where heat radiation is included and excluded.

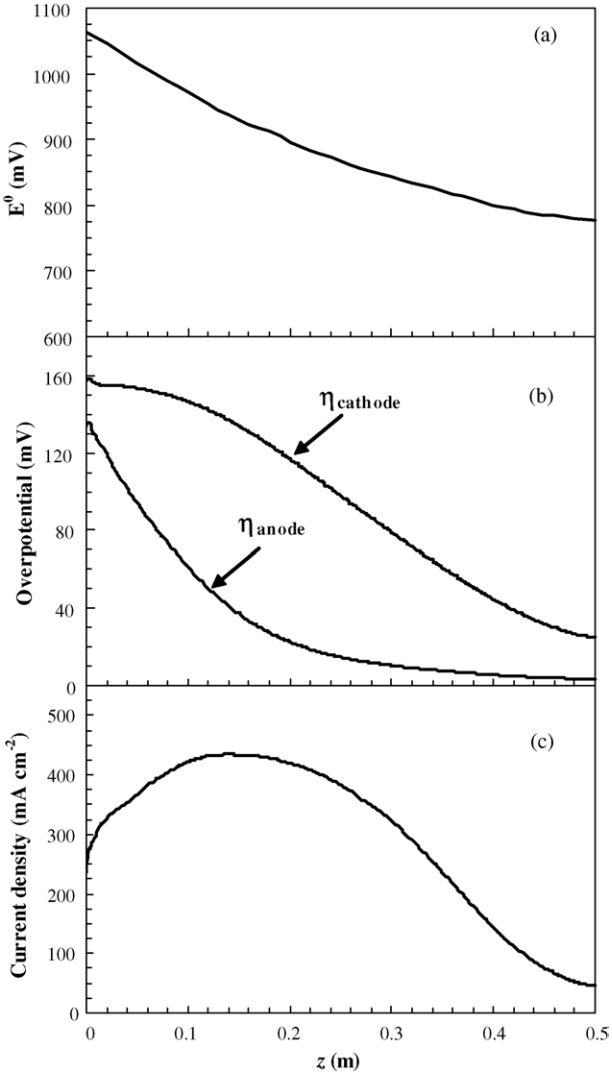

Fig. 10. Distributions of E^0 (a), overpotential (b) and current density (c) along the cell length for the base case model ($I_E \sim 300\,mA\,cm^{-2}$, $V_{cell} = 0.7$ V, $U_{air} \sim 0.167$ and $U_{fuel} \sim 0.85$).

fuel channel and cell structure is quite uniform primarily due to high thermal conductivity of the electrode material. With regard to the axial direction, the temperature within the fuel channel reaches a maximum of about ~1110 °C near the centre of the cell, which is ~230 °C greater than the inlet fuel temperature. Therefore, this region requires particular attention since the electrode material can crack due to the stress created by hot spots.

The three mechanisms that drive heat from the cell to the air are conduction, convection and radiation. Radiative effects are significant only when the operating temperature is quite high, as in a SOFC. Fig. 8 shows the amount of heat radiated from the cell surface to the surface of the air-preheating tube. Near the fuel inlet, the temperature difference between the air-preheating tube and the cell is low enough that only a small amount of heat is transferred to the air-preheating tube. On the other hand, it is relatively uniform between $z \sim 0.26$ and ~0.34 m where the temperature difference between the air-preheating tube and the cell is relatively constant. At an axial distance greater than ~0.34 m, the rate of radiative heat transfer decreases slightly from ~700 to ~550 W m^{-2} before drastically increasing from ~550 to ~1450 W m^{-2} in the fuel outlet region. The high radiation rate at $z \sim 0.5$ m is caused by the large temperature difference between the cell and the inlet air and makes an important contribution to air preheating. Fig. 9 compares the cell temperature profiles in the cases where the radiative heat transfer is included and where it is not and indicates that its inclusion leads to a decrease in the cell temperature of ~60 °C near the centre of the cell. This temperature difference is relatively small because heat convection in the air channel is the predominant mode of heat transfer. The contribution of heat radiation should increase as the air velocity is reduced. Although the temperature difference seems small when compared to the operating temperature, it is still critical for the heat management since the extra amount of heat generated inside a cell can cause material degradation.

3.2.3. Distributions of reversible cell potential, overpotential and current density

Fig. 10 illustrates the distributions of the reversible cell potential (E^0), overpotentials and current density along the cell length. E^0 decreases along the cell length because of the depletion of fuel and oxidant downstream. The reversible

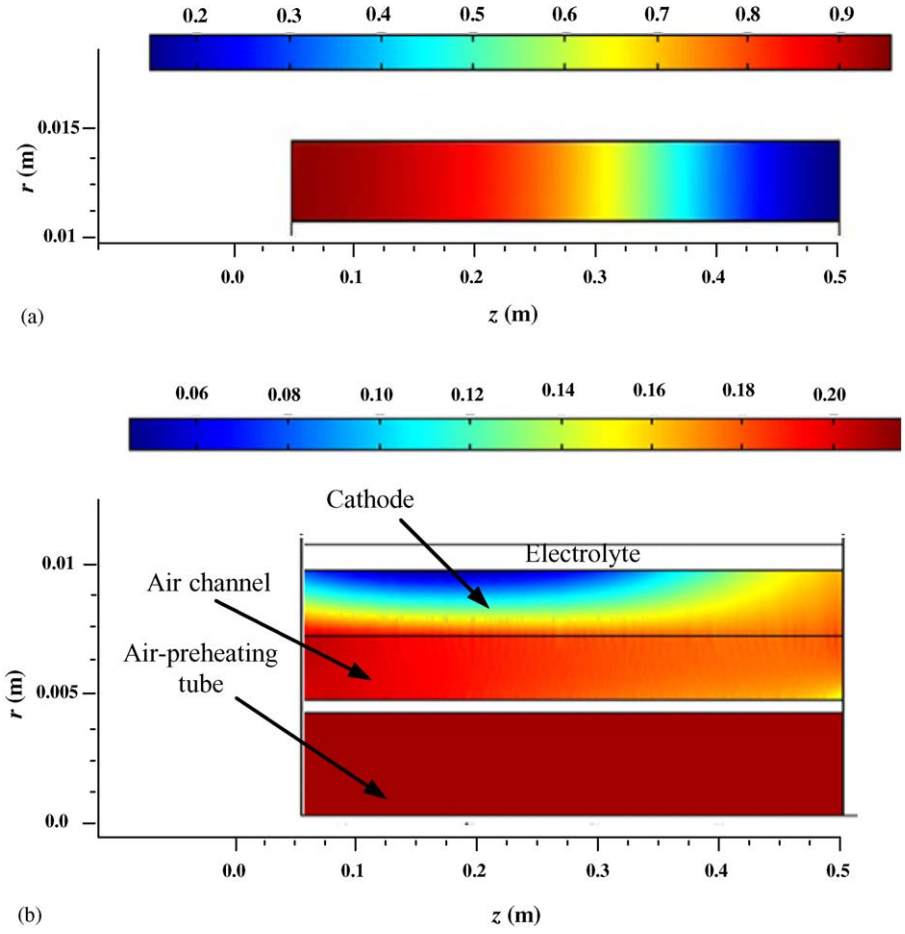

Fig. 11. Surface plots of distributions of H_2 (a) and O_2 (b) concentrations for the base case model ($I_E \sim 300$ mA cm^{-2}, $V_{cell} = 0.7$ V, $U_{air} \sim 0.167$ and $U_{fuel} \sim 0.85$). Concentrations are expressed in terms of molar fractions.

cell potential at the fuel outlet is about 73% of that at the inlet end. This implies that the reduction of the reversible cell potential is one of the major reasons for decreasing cell performance. On the other hand, the overpotentials at the cathode and the anode decrease as one moves away from the fuel inlet. In general, the overpotential increases as the current density rises. Nonetheless, the overpotentials still decrease even when the current density increases in the region from $z = 0$ to ~ 0.2 m. The reason is that the effect of increasing current density is more than compensated by the concomitant increase in temperature (see Fig. 7), which leads to a decrease of overpotential. Moreover, the overpotential at the cathode side is greater than that at the anode side over the entire length of cell because of inherently slower kinetics of the cathodic reaction and large cathode thickness [8].

As shown in Fig. 10(c), the current density increases and reaches a maximum of $\sim 440\,\mathrm{mA\,cm^{-2}}$ at an axial distance of ~ 0.14 m. Thereafter, it continuously decreases toward the fuel cell outlet. The minimum current density is $\sim 50\,\mathrm{mA\,cm^{-2}}$ at the tube outlet. The key parameters affecting the electrochemical reaction rate are the local H_2 concentration and temperature. At the fuel cell inlet, high H_2 concentration results in a high reaction rate. The current density keeps increasing although H_2 concentration decreases along the fuel inlet region because of an increase in the local temperature as depicted in Fig. 7. Beyond $z \sim 0.14$ m, the current density decreases while the local temperature is still increasing since the influence of H_2 depletion affects the current density more strongly than the local temperature.

3.2.4. Distributions of species concentrations

The distributions of H_2 and O_2 concentrations within the cell are displayed in Fig. 11. The H_2 concentration is quite uniform in the radial direction over the entire length of the cell because of the high H_2 diffusivity (Fig. 11(a)). On the other hand, O_2 concentration at the reaction site (cathode/electrolyte interface) is much lower than its bulk concentration especially at the axial position where the high current density is observed (Fig. 11(b)). This is likely due to the fact that O_2 diffuses relatively slowly through the porous cathode. As a result, the overall cell performance of a cathode-supported tubular SOFC is limited by the O_2 diffusion through the thick porous cathode. Therefore, the use of a cell with a very thin cathode such as the recently developed high power density solid oxide fuel cell (HPD-SOFC) [27] should be able to overcome this problem.

4. Conclusions

A mechanistic model of a cathode-supported tubular SOFC that includes charge, momentum, mass and heat transport has been developed. In this way, it avoids using correlations for calculating heat and mass transfer coefficients which may result in large errors. The model also includes the effect of heat radiation between the cell and the air-preheating tube.

The model shows good agreement with experimental current–potential curve data obtained from the literature. The distribution plots of flow, temperature, current density and species concentrations contribute to a better understanding of transport phenomena inside the cell. The model results suggest that O_2 diffusion through the thick porous cathode limits the cell performance of a tubular-type SOFC.

Acknowledgements

Financial support by the Canadian Program for Energy Research and Development (PERD) and the CANMET CO_2 consortium is gratefully acknowledged.

References

[1] S.C. Singhal, Advances in solid oxide fuel cell technology, in: Proceedings of the 1998 Fuel Cell Seminar, Courtesy Associates, November 1998.
[2] S. Campanari, J. Power Sources 92 (2001) 26.
[3] S. Nagata, A. Momma, T. Kato, Y. Kasuga, J. Power Sources 101 (2001) 60.
[4] P. Aguiar, D. Chadwick, L. Kershenbaum, Chem. Eng. Sci. 57 (2002) 1665.
[5] P. Aguiar, D. Chadwick, L. Kershenbaum, Chem. Eng. Sci. 59 (2004) 87.
[6] P. Li, M. Chyu, J. Power Sources 124 (2003) 487.
[7] P. Li, K. Suzuki, J. Electrochem. Soc. 151 (2004) A548.
[8] S.H. Chan, K.A. Khor, Z.T. Xia, J. Power Sources 93 (2001) 1130.
[9] P. Costamagna, K. Honegger, J. Electrochem. Soc. 145 (1998) 3995.
[10] M. Iwata, T. Hikosaka, M. Morita, T. Iwanari, K. Ito, K. Onda, Y. Esaki, Y. Sakaki, S. Nagata, Solid State Ionics 132 (2000) 297.
[11] S. Campanari, P. Iora, J. Power Sources 132 (2004) 113.
[12] A. Hagiwara, H. Michibata, A. Kimura, M.P. Jaszcar, G.W. Tomlins, S.E. Veyo, Proceedings of the Third International Fuel Cell Conference, D2-4, 1999, p. 369.
[13] J.R. Ferguson, J.M. Fiard, R. Herbin, J. Power Sources 58 (1996) 109.
[14] R.R. Bird, W.E. Stewart, E.N. Lightfoot, Transport Phenomena, second ed., John Wiley & Sons, New York, 2002.
[15] R.C. Reid, J.M. Prausnitz, B.E. Poling, The Properties of Gases and Liquids, fourth ed., McGraw-Hill, New York, 1987.
[16] R. Krishna, J.A. Wesslingh, Chem. Eng. Sci. 52 (6) (1997) 861.
[17] E.A. Mason, A.P. Malinauskas, Transport in Porous Media: The Dusty-Gas Model, Elsevier, New York, 1983.
[18] R. Suwanwarangkul, E. Croiset, M.W. Fowler, P.L. Douglas, E. Entchev, M.A. Douglas, J. Power Sources 122 (2003) 9.
[19] J. Bear, Dynamics of Fluids in Porous Media, Elsevier, New York, 1972.
[20] R.E. Williford, L.A. Chick, G.D. Maupin, S.P. Simner, J.W. Stevenson, J. Electrochem. Soc. 150 (8) (2003) A1067.
[21] H.D. Do, D.D. Do, Chem. Eng. Sci. 53 (6) (1998) 1239.
[22] E.A. Avallone, T. Baumeister, Mark's Standard Handbook for Mechanical Engineers, 10th ed., McGraw Hill, New York, 1996.
[23] R. Tang, Y. Etzion, I.A. Meir, Energy Convers. Manage. 45 (2004) 1831.
[24] COMSOL Ltd., FEMLAB® Version 3.0 User's Guide, COMSOL, Boston, 2004.
[25] M.F. Modest, Radiative Heat Transfer, second ed., Elsevier, California, 2003.
[26] L. Petruzzi, S. Cocchi, F. Fineschi, J. Power Sources 118 (2003) 96.
[27] S.C. Singhal, Solid State Ionics 135 (2000) 305.